

Tiny particles building huge ore deposits – Particle-based crystallisation in banded iron formation-hosted iron ore deposits (Hamersley Province, Australia)

Mathias S. Egglseder^{a,b,*}, Alexander R. Cruden^a, Andrew G. Tomkins^a, Siobhan A. Wilson^{a,c}, Hilke J. Dalstra^d, Andrea Rielli^a, Chenghao Li^b, Jens Baumgartner^b, Damien Faivre^b

^a School of Earth, Atmosphere and Environment, Monash University, Melbourne, Victoria 3800, Australia

^b Department of Biomaterials, Max Planck Institute of Colloids and Interfaces, Science Park Golm, 14424 Potsdam, Germany

^c Department of Earth and Atmospheric Sciences, University of Alberta, Edmonton, Alberta T6G 2E3, Canada

^d Rio Tinto Exploration, 37 Belmont Avenue, Belmont, WA 6104, Australia

ARTICLE INFO

Keywords:

Banded iron formation
Iron ore
Hematite
Non-classical crystallisation
Nanoparticles
Hamersley Province

ABSTRACT

The world's major source of iron ore is hosted in Precambrian banded iron formations. These chemical (meta-) sedimentary rocks are composed of alternating laminae of iron oxide minerals and chert. Despite the economic significance of high-grade iron ore deposits, controversy persists after decades of research on how banded iron formations became upgraded to form iron ore. The fundamental requirement for iron ore formation is the removal of vast amounts of chert coupled with an increased concentration of iron oxide minerals.

Here, we assess the fate of colloidal hematite inclusions encapsulated in chert after quartz dissolution and examine their role in the formation of hematite ore. We have analysed hematite ores from the Hamersley Province (Australia) using a combination of petrography, high-resolution electron microscopy and X-ray diffraction. These techniques reveal the presence of abundant nano and microscale hematite particles that we suggest form the building blocks of larger hematite crystals within the iron ore. Our textural observations indicate that hematite colloids that were previously encapsulated inside the microcrystalline quartz grains in chert layers are released during quartz dissolution, and subsequently reassemble in a self-similar fashion to form new microplaty hematite crystals via non-classical crystallisation pathways. Progressive growth and fusion leads to the transformation of hematite microplates into hematite bands, which resemble pre-existing iron oxide laminae of banded iron formations. In contrast to previous models, we observe the direct transformation of banded iron formations to microplaty hematite and have not found evidence that significant amounts of hematite formed through metamorphism of goethite or that intermediate carbonate minerals were involved during the upgrading of banded iron formations to pure hematite ore.

Given the strong evidence for hypogene fluids found in many deposits, we have also assessed the role that such warm, highly saline fluids may have played during the evolution of iron ore. Using insights from crystal chemistry we conclude that fluid infiltration impacts many aspects of iron ore formation by controlling hematite colloid liberation and aggregation, and finally controlling the transformation of the colloids into macroscopic crystals of hematite via non-classical crystallisation mechanisms. Our study underlines the significance of hypogene fluids in the upgrading of banded iron formation to iron ore, however, we suggest that their influence was mainly passive as hematite was not precipitated directly from these fluids.

1. Introduction

Banded iron formations (BIF) provide key information about the nature of the Precambrian atmosphere and hydrosphere and the global rise of oxygen; they also contain large volumes of high-grade iron ore

(Bekker et al., 2010; Hagemann et al., 2016). BIF are composed of alternating layers of iron oxide minerals and chert, and debate exists on how BIFs (30–35% Fe) are upgraded to residual BIF-hosted high-grade (> 55% Fe) bedded iron ore deposits (BIDs) (Hagemann et al., 2016; Morris and Kneeshaw, 2011). One type of such residual deposits in the

* Corresponding author at: Department of Biomaterials, Max Planck Institute of Colloids and Interfaces, Science Park Golm, 14424 Potsdam, Germany.
E-mail address: egglseder.mathias@gmail.com (M.S. Egglseder).

<https://doi.org/10.1016/j.oregeorev.2018.10.001>

Received 2 January 2018; Received in revised form 22 March 2018; Accepted 10 October 2018

Available online 13 October 2018

0169-1368/© 2018 Elsevier B.V. All rights reserved.

Hamersley Province, northwest Australia are termed microplaty hematite deposits, where hematite ore genesis occurs by selective removal of gangue minerals including quartz, carbonates and iron silicates and formation of secondary μm -sized hematite platelets (i.e., microplaty hematite) (Hagemann et al., 2016; Morris and Kneeshaw, 2011; Taylor et al., 2001).

Precursor BIF and iron ore are chemically and texturally similar around the world and there is strong evidence for the involvement of diverse fluids in the upgrading of BIFs to BIDs (e.g., Hagemann et al., 2008, 2016). However, it is remarkable that these chemically diverse fluids all resulted in the same ore type, despite different chemical reaction pathways. This phenomenon is probably unique to the BID system. Major questions have been raised about the genesis of the Australian Hamersley Province BIDs, including the ability of the postulated fluids to account for the required mineral replacement reactions, the fate of dissolved quartz, the source of iron required to precipitate microplaty hematite, and the documented correlation between mineralisation and deformation events (Kneeshaw and Kepert, 2002; Morris and Kneeshaw, 2011; Rasmussen et al., 2007; Taylor et al., 2001). Although microplaty hematite has been the focus of detailed microscopic studies (e.g., Morris, 2012), nanoscale features of hematite within these ores have not been investigated in detail.

A recent wave of nanoscale studies have triggered a new debate about the controversial origin of BIF, in particular whether iron oxides or iron silicates were the primary iron phase during the formation of BIFs (Rasmussen et al., 2016, 2015; Sun et al., 2015; Sun and Li, 2017). These studies base their interpretations on abundant colloidal mineral inclusions in quartz that render chert layers from green to red in colour (e.g., jasper) (The term ‘colloid’ refers to a phase that has at least one dimension in the nanometre range, which is dispersed in another phase of different composition or state). Although it is widely accepted that vast amounts of quartz were removed from BIFs during ore genesis to produce BIDs, the fate of the large quantities of mineral inclusions that were originally hosted within chert has not been addressed to date.

Here, we attempt to resolve what happens to these encapsulated hematite colloids after quartz dissolution and whether processes involving hematite particles were present in BIDs, through a combination of light and electron microscopy, and X-ray diffraction techniques. Furthermore, we address the formation mechanism of microplaty hematite and evaluate the concomitant effects of the proposed ore forming fluids on Hamersley Province BIF during iron ore genesis. Our study provides an alternative model for microplaty hematite formation. We suggest that hematite particles are the major building blocks of iron ore minerals in BIDs of the Hamersley Province instead of iron-rich solutions, which has important implications for crystallisation mechanisms and pathways, in the genesis of iron ore deposits.

2. Geological overview

2.1. Regional geology

The Hamersley Province in northwest Australia is a major iron ore district and currently holds > 50 Gt of iron ore (Fig. 1). The most economic BIF units are the Marra Mamba Iron Formation, Dales Gorge Member and Joffre Member of the Brockman Iron Formation (Fig. 1). These units are interbedded with dolomitic shales of the Wittenoom Formation and shaly units of the Mount Sylvia Formation, Mount McRae Shale Formation and Whaleback Shale Member. Some of the largest high-grade iron ore deposits (up to 2 Gt) are hosted in Dales Gorge Member BIF and are located at Mount Tom Price, Paraburdoo and Mount Whaleback (Fig. 1; Morris and Kneeshaw, 2011).

BIFs are well known for their characteristic layering on macro-, meso- and microbanding scales (Trendall et al., 2004; Trendall and Blockley, 1970). Macrobands consist of m-scale BIF packages separated by cm- to m-thick shale macrobands of volcanoclastic origin (Pickard, 2002; Trendall and Blockley, 1970). BIF itself comprises alternating cm-

thick mesobands and mm- to μm -thick microbands of mainly chert and iron oxides (Trendall and Blockley, 1970). Hamersley Province BIF have been affected by low-grade burial metamorphism and the province has been deformed by three major compressional events intermitted by extensional events resulting in a locally complex fold and fault network (Dalstra, 2014, 2006; Smith et al., 1982; Taylor et al., 2001).

2.2. Iron ore

BIDs of the Hamersley Province are strata-bound and are generally considered to form *in situ* by sequential leaching of gangue minerals (i.e., quartz, carbonates, silicates, apatite) from the host rock, commonly requiring ~ 50 vol% of the BIF to be replaced and/or removed by fluids (Morris, 1980; Taylor et al., 2001). Most deposits consist predominantly of oxidised hematite or hematite-goethite ore bodies with relatively pure ores. These are dominated by iron oxides and iron oxyhydroxides (> 64 wt% Fe) with minor amounts of aluminium and silica (< 1 wt%), and traces of apatite and manganese oxide (Morris, 1985; Taylor et al., 2001).

BID ores can be subdivided into lower grade (58–62 wt% Fe) Martite–Goethite ore (M-G) and less abundant premium (58–67 wt% Fe) Martite–microplaty Hematite (M-mplH) ores. “Martite” is a term introduced by the iron ore community for the pseudomorphic replacement of magnetite by hematite, and is commonly used to describe euhedral hematite crystals in BID ore with the exception of microplaty hematite (e.g., Morris, 1980). The petrology of BID ores is relatively simple with bands of hematite with randomly oriented interstitial goethite or microplaty hematite occupying the space of the leached gangue minerals (Fig. 2a–c).

The most characteristic features of the Hamersley Province BID ore are (1) the preservation of banding at all scales, having been retained from the parent BIF, and (2) that iron oxide layers can commonly be traced laterally from the BID into unmineralised BIF (e.g., MacLeod, 1966; Morris and Kneeshaw, 2011). Sharp transitions of ore to BIF are commonly observed without separating structures or alteration zones (Lascelles, 2012; Morris, 1985). The final ores are highly porous (~ 20–30%) and are usually accompanied by significant stratigraphic thinning of the host BIF formation (~ 35–50%; Taylor et al., 2001). Evidence for hydrothermal or metamorphic alteration associated with M-G type ore has not been identified, and previous work suggests that no particular structural or stratigraphic setting controlled ore formation (Lascelles, 2012). M-G ore grades vary between 58 and 63 wt% Fe with varying P levels and it is widely acknowledged that they formed due to supergene weathering as they are bound to the present land surface (e.g., Morris and Kneeshaw, 2011). However, in this study we focus on the formation of M-mplH ores, which are typically hard, massive or friable blue-grey ores comprising hematite bands and randomly oriented microplaty, bladed or anhedral hematite that fills the space left behind by removal of gangue minerals (i.e. quartz) (Fig. 2) (e.g., Morris, 2012; Thorne et al., 2008). M-mplH ores show a wide range of grain sizes, shapes and intergrowths of both hematite bands and microplates, leading to strong microscale textural variations across different deposits and continents (Morris, 2012). This ore type is mostly free of goethite and commonly shows small-scale folding or local brecciation (Fig. 2a) (Dalstra and Guedes, 2004; Morris and Kneeshaw, 2011). M-mplH ore bodies typically extend to much greater depths (> 400 m) than the M-G ores and are usually associated with normal faults or second order folds (Dalstra, 2006; Taylor et al., 2001).

2.3. Iron ore genesis models

Many genesis models have been proposed to explain the upgrading of BIF to high-grade M-mplH ore ranging from supergene, hypogene and combined supergene/hypogene models to syntectonic and syngenetic models (see reviews by Hagemann et al., 2016; Morris, 1985; Morris and Kneeshaw, 2011). However, no model can explain all of the

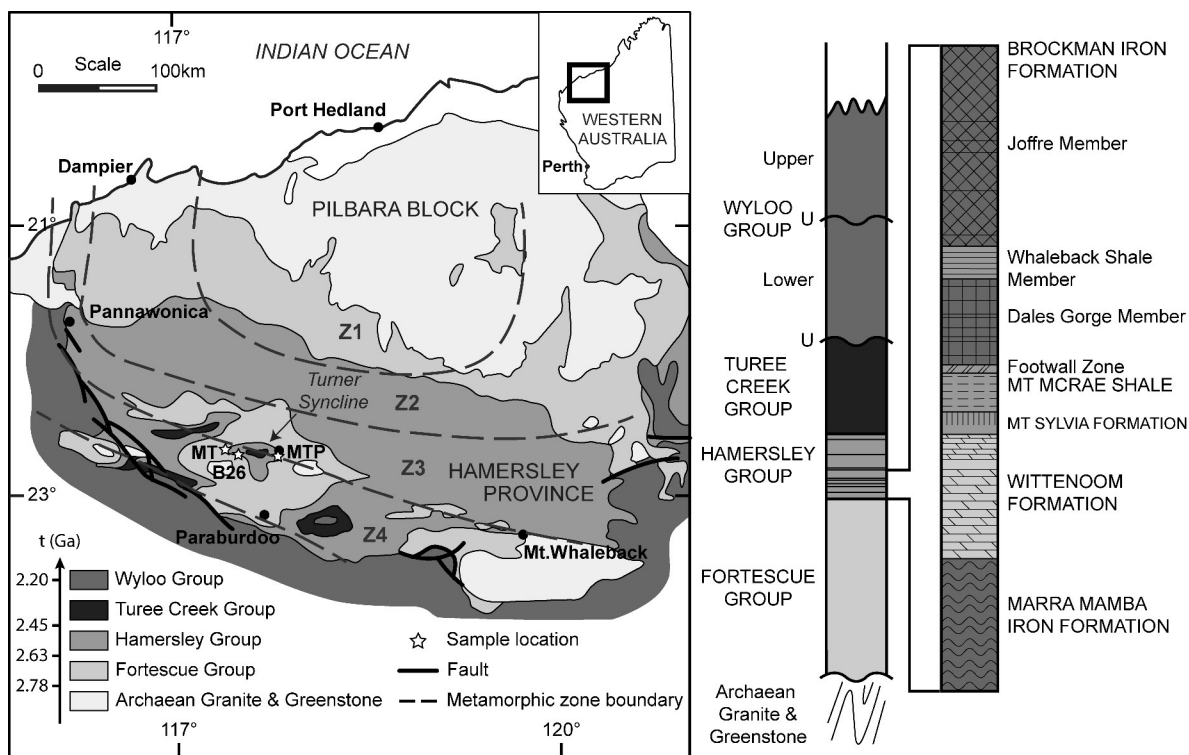


Fig. 1. Geological overview of the Hamersley Province. The Mount Tom Price deposit is located at the eastern end of the Turner Syncline, Mount Turner at the western end respectively (modified after Taylor et al., 2001). Ages (t) are based on Trendall et al. (2004) and metamorphic zones are identified as Z1: prehnite-pumpellyite facies, high zeolite facies; Z2: prehnite-pumpellyite-epidote facies; Z3: pumpellyite-actinolite facies; Z4: greenschist zone (Smith et al., 1982). MT: Mt. Turner; MTP: Mt. Tom Price.

main features of M-mplH ores, specifically the preservation of pre-existing iron oxide microbands, the removal of vast amounts of quartz, sharp transitions from BIF to high-grade iron ore, the high porosity of the ores and a lack of extensive wall rock alteration due to fluid infiltration (e.g., Morris and Kneeshaw, 2011).

Morris (1980) and later research (e.g., Morris, 2003, 1985; Morris and Fletcher, 1987; Morris and Kneeshaw, 2011) proposed that Hamersley Province M-G deposits formed close to Earth's surface during the Paleoproterozoic and that later low-grade burial metamorphism (~80–100 °C) led to dehydration of the interstitial goethite to hematite microplates, which make up the M-mplH ore. Additionally, the conversion of goethite to hematite would involve a ~27 vol% reduction, accounting for the high porosity of the ores (Morris, 2012, 2003). More recent models are based on quantitative geochemical, fluid inclusion and stable oxygen isotope data obtained from rare occurrences of calcareous alteration zones and veins that record the presence of hypogene brines in fluid inclusions (Barley et al., 1999; Brown et al., 2004; Taylor et al., 2001; Thorne et al., 2009, 2014, 2004; Webb et al., 2004). The hypogene/supergene model emerged from these observations; it proposes multi-stage ore genesis that began with the removal of chert and partial replacement of quartz by siderite precipitated from hypogene fluids (Taylor et al., 2001). This overprint resulted in a 'protore' mainly composed of magnetite and Fe-carbonate minerals (Taylor et al., 2001; Thorne et al., 2006). The hypogene fluids were highly-saline (18–40 wt %, NaCl–CaCl₂-equiv.; Ca > Na > K) and warm (110 to 420 °C), and possibly interacted with the dolomitic units of the Wittenoom Formation or alternatively with evaporitic brines from the surface (Taylor et al., 2001; Thorne et al., 2014, 2006, 2004). Although, Powell et al. (1999) previously considered these fluids to have been oxidizing, they are now generally believed to have been reducing (Taylor et al., 2001). This latter model proposes that the initial stage of ore formation was followed by an influx of heated supergene fluids that oxidised the metasomatised BIF and formed microplaty hematite with ankerite

(Taylor et al., 2001; Thorne et al., 2014, 2008, 2004). Lastly, modern weathering would have removed the remaining carbonate minerals and apatite resulting in high-grade, pure and porous hematite ore (Taylor et al., 2001; Thorne et al., 2008).

Normal faults are a key element in this model as they are thought to have acted as conduits for ascending or descending fluid flow into the BIF (Evans et al., 2013; Taylor et al., 2001; Thorne et al., 2014, 2008). However, it has been shown recently that some normal fault structures formed during regional shortening events, rather than regional extension due to *syn*-folding localised shearing, which has important implications for the structural evolution of the deposits (Egglseder et al., 2017). M-mplH ores are not schistose, therefore it is commonly assumed that there was no tectonic contribution to ore mineralisation. However, it has been shown that microplaty hematite formed during all major regional deformation events (Rasmussen et al., 2007) and that deformation is controlled by fluid-assisted dissolution-precipitation creep, which can lead to relevant remobilisation of quartz from micro-to deposit scales (Egglseder et al., 2017, 2016).

Morris (2003, 2002) and Morris and Kneeshaw (2011) reject the hypogene/supergene model and consider the metasomatised residuals to be post-ore phenomena. Further, they question the chemical ability and availability of the proposed fluids to account for the observed removal of ~50% of the rock volume. Even supporters of the hypogene/supergene concept have noted that carbonate alteration may not necessarily be a prerequisite for hypogene upgrading of BIF to iron ore; however, they do not provide an alternative mechanism for microplaty hematite formation without carbonate replacement (Hagemann et al., 2016). Extensive host rock alteration along proposed fluid pathways has not been observed in M-mplH ores, which is another unsolved feature of the hypogene/supergene model (Morris and Kneeshaw, 2011). Supporters of the hypogene/supergene model do not infer an external source for the iron required to crystallise microplaty hematite. However, they do not specify the exact location of this source of iron or

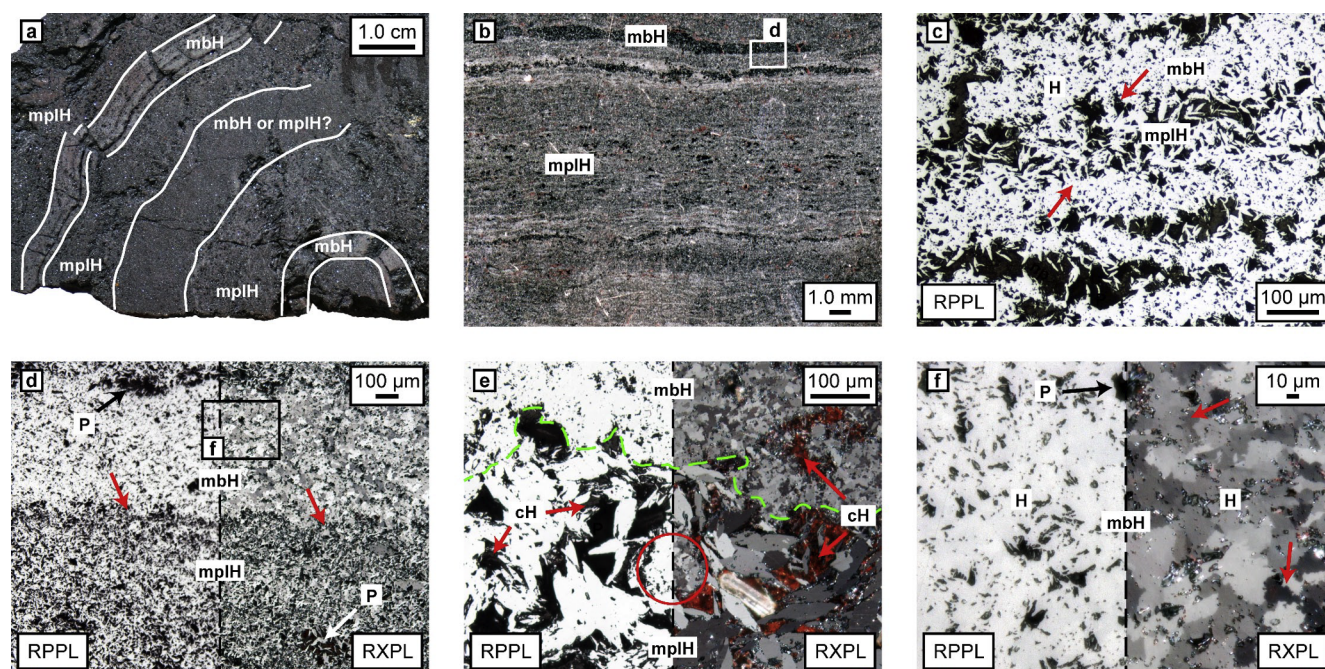


Fig. 2. M-mplH ore textures. a) Specimen of M-mplH ore showing deformed meso- and microbands of hematite. The bands (white lines) show layer-dependent porosity and strong grain size variation, which can make it difficult to differentiate between a pre-existing iron oxide band, or a band of microplaty hematite. b) Microbands of hematite with fine-grained interstitial microplaty hematite with high porosity. c) Porous microbands of hematite with irregular boundaries (arrows) and interstitial, randomly oriented microplaty hematite. The porosity (black) of microplaty hematite domains is commonly filled with hematite particles (dark grey). d) Close-up of a hematite microband and a layer of microplaty hematite. The boundary between them is highly irregular, and RXPL reveals a complex inequigranular and interlobate texture of anhedral hematite crystals in the microband. e) Irregular boundaries (dashed line) between microplaty hematite and microbanded hematite showing that microplates did not nucleate on the microbands. Examination in RPPL and RXPL reveals that microplates are randomly oriented, commonly do not show internal textures, and are associated with large porosity (black) that is regularly filled by hematite particles (orange/red). In contrast, microbands are composed of a fine-grained mosaic of anhedral hematite crystals and show less intergranular porosity. An aggregate of anhedral hematite crystals inside the microplaty network (circle) shows the same textures as the hematite microbands. f) Close-up of hematite microband in (d). RPPL shows only high amounts of porosity, however RXPL reveals complex inequigranular to seriate and interlobate to amoeboid textures of anhedral hematite crystals with high-energy grain boundaries (arrows) and significant intergranular porosity. cH: colloidal hematite/hematite particles, H: hematite, mbH: microbanded hematite, mplH: microplaty hematite, P: porosity, RPPL: reflected plane polarized light, RXPL: reflected crossed polarized light.

provide a feasible mechanism for microplaty hematite formation (Kneeshaw and Kepert, 2002; Morris, 2003; Morris and Kneeshaw, 2011; Taylor et al., 2001; Thorne et al., 2014).

2.4. Non-classical crystallisation

Existing iron ore genesis models and inferred accompanied crystallisation processes are based on the ‘classical’ concept of crystal formation, which suggests that crystals form by layer-wise addition of monomeric chemical species (i.e. atoms/ions/molecules) to a crystal nucleus (Burton et al., 1951). However, advancements in crystal synthesis and analytical techniques over the last 20 years have found that many crystals form alternatively from complexes or solid nanoparticles/colloids; a mechanism termed non-classical crystallisation, crystallisation by particle attachment, or oriented attachment (Cölfen and Antonietti, 2008; De Yoreo et al., 2015; Fang et al., 2011; Liu et al., 2014; Penn et al., 2001; Penn and Banfield, 1998). It has been shown that crystals formed by such processes require an amended framework to the classical nucleation theory to be described. Hence, classical interpretations of crystallisation mechanisms and conditions in the laboratory and environment have been challenged (Baumgartner and Faivre, 2015). Recently, multiple studies have revealed that iron oxides can also form via aggregation-based scenarios, which has resulted in major breakthroughs in environmental-, material- and nanosciences (Baumgartner and Faivre, 2015; Faivre, 2016; Guo and Barnard, 2013; Niederberger and Cölfen, 2006; Penn et al., 2001; Rout et al., 2014). However, adoption of this paradigm shift to iron oxides in rocks is yet to occur and here we aim to determine whether microplaty hematite in

BIDs of the Hamersley Province formed by classical or non-classical crystallisation mechanisms.

3. Samples and methods

We analysed BIF samples from the Turner Syncline in the central part of the Hamersley Province (Fig. 1), and M-mplH ore samples from the Mount Tom Price deposit and the Mount Turner deposit at the eastern and western end of the Turner Syncline respectively. M-mplH samples originate from the deepest parts of the South East Prongs ore body, an active mining area in the Mount Tom Price deposit (Egglseder et al., 2017), which is far removed from the influence of surficial weathering. In contrast, specimens from the Mount Turner were sampled from surface outcrops, and have therefore not been included in our petrographic studies. We combined ore petrography and scanning and transmission electron microscopy (SEM, TEM) supported by X-ray diffraction (XRD) analyses. SEM was conducted using a JEOL 7001F FEG-SEM with an energy dispersive X-ray spectrometer (EDS) operated at an accelerating voltage of 15 kV and a probe current of 1.1 nA, and a JEOL 7500F FEG-SEM with EDS at an accelerating voltage of 5–15 kV and a probe current of 10 µA. TEM samples were produced mechanically and consist of fragments of targeted microplaty hematite layers, and imaged using a double-corrected JEOL ARM200F, equipped with a cold field emission gun. For the investigation, the acceleration voltage was put to 200 kV and the emission was set to 15 µA. With these settings, the microscope reaches a lattice resolution of about 1 Å.

We employed careful sample preparation techniques using ultrasonic cleaners to avoid any sample preparation artefacts resulting from

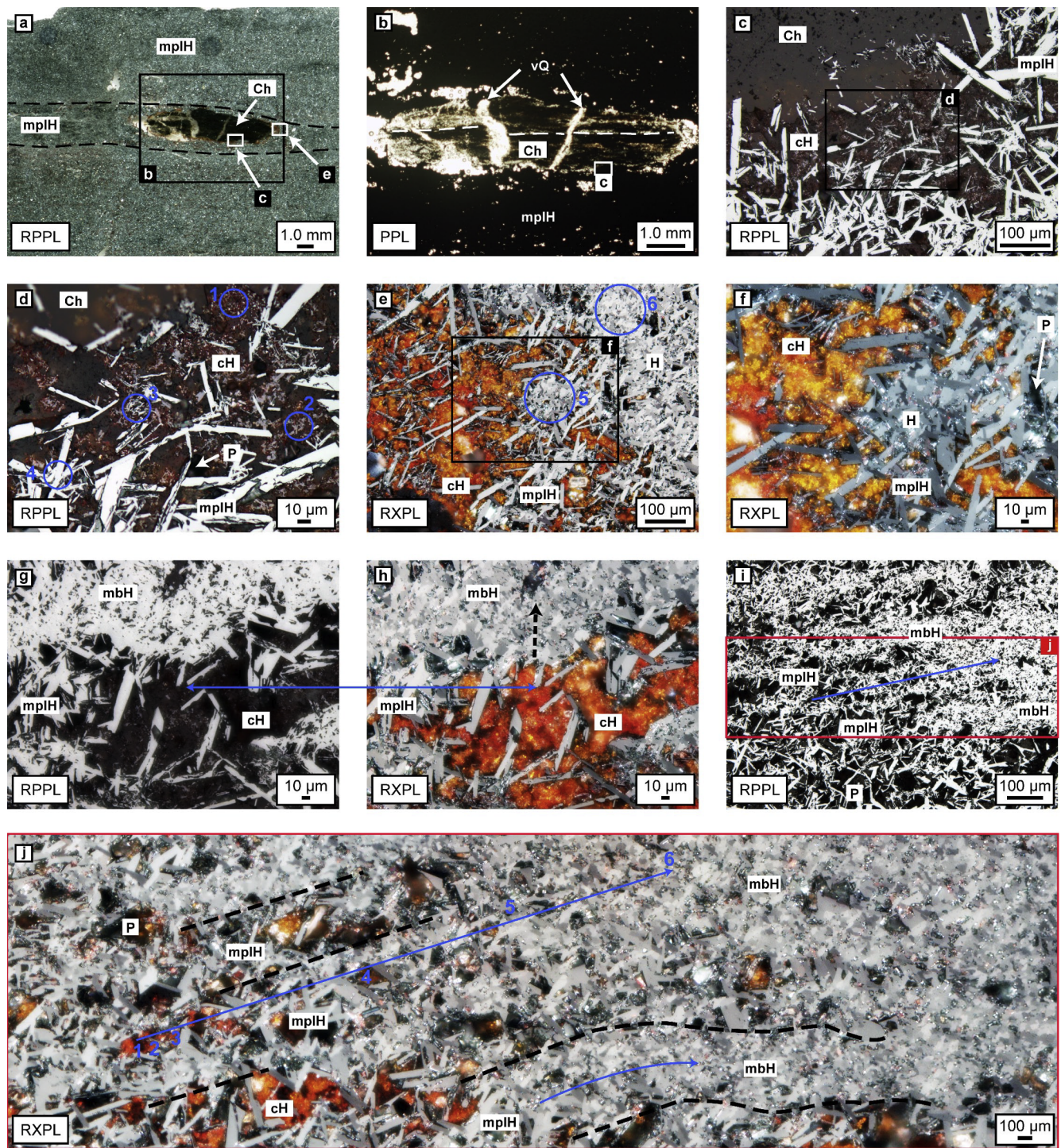


Fig. 3. Transition from chert to M-mplH ore. a) Progressive transformation of a chert relic to microplaty hematite. The texture of the pre-existing chert band is still preserved in the hematite bands (dashed line). b) Close-up of the chert relic, with visible banding (dashed line) and dark coloration due to abundant encapsulated hematite colloids. The relic is crosscut by quartz veins that do not continue into the adjacent microplaty hematite mineral assemblage. c, d) The contact zone between chert and microplaty hematite is occupied by a matrix of hematite particles with faint red internal reflections in RPPL. Inside this matrix, microplaty hematite crystals have nucleated (1) and have grown continuously in random directions (2–4). e, f) RXPL reveals distinct orange to red internal reflections of the matrix composed of abundant hematite particles. Progressive intergrowth of microplaty hematite led to the loss of the microplaty habit (5) and eventually resulted in an irregular texture of anhedral hematite crystals (6). g, h) Comparison of the particle – microplaty hematite – anhedral hematite transition in RPPL (g) and RXPL (h). The grain size of hematite crystals within microbands increases outwards towards the irregular boundary with the microplaty hematite and hematite particle matrix. i) Lateral transition of microplaty hematite into hematite microbands (arrow). j) Close-up of (i) showing the lateral transition of microplaty hematite into hematite microbands and finally to a hematite mesoband (arrow). Microplaty hematite crystals grew in a matrix of hematite particles (1 to 4) and progressive intergrowth of the microplates led to modification of the texture to produce fine-grained anhedral hematite and a reduction in porosity (5, 6) resulting in the formation of new hematite micro- and mesobands with low porosities that are virtually free of hematite particles. cH: colloidal hematite/hematite particles, Ch: chert, H: hematite, mbH: microbanded hematite, mplH: microplaty hematite, P: porosity, vQ: quartz vein, R-PPL: reflected plane polarized light, R-XPL: reflected crossed polarized light.

cutting or polishing. Further to this, we compared textures in polished versus unpolished samples and embedded samples with unembedded samples. We are therefore confident that all microstructural and mineralogical observations described are genuine and not due to sample preparation artefacts.

Quantitative powder X-ray diffraction (PXRD) data were collected using a PANalytical MPD diffractometer with a Co X-ray tube operated at 40 kV and 40 mA over a range of 5 to 140° (2 θ) using a X'Celerator linear position sensitive detector and a Bruker AXS D8 Advance diffractometer with a Sol-X energy dispersive X-ray detector over a range of 10 to 100° (2 θ) using a vertical θ - θ goniometer with parallel beam optics. Powder samples were obtained from different bands (chert, hematite, microplaty hematite) within individual samples by cutting mm-sized blocks that were subsequently milled. Spatially resolved XRD data (SRXRD) were collected from thin sections (approximate thickness: 50 μ m) in transmission mode at the μ -Spot beam line, BESSY II, Berlin (Germany) with an incident beam wavelength of $\lambda = 0.82656$ Å, a Si (1 1 1) monochromator and a beam spot size of 50 μ m (Paris et al., 2007).

Modal mineralogy results were obtained from PXRD data with the Rietveld method (Bish and Howard, 1988; Hill and Howard, 1987; Rietveld, 1969) using the program Topas v.4.2 from Bruker AXS and the fundamental parameters approach (Cheary and Coelho, 1992) and the program Match v.3.5 from Crystal Impact, which employs the FullProf algorithm (Rodríguez-Carvajal, 2001) to perform Rietveld refinements. SRXRD data were processed using DPDAK software (Benecke et al., 2014) using the following plugins: Image Logger, ImageIntegrationSubBG, and L_param. The obtained XRD data were used to determine hematite crystallite sizes (L) from the breadth of diffraction peaks, which become broader with decreasing crystallite size using Scherrer's equation (Patterson, 1939a, 1939b),

$$L = \frac{k\lambda}{B\cos\theta} \quad (1)$$

which relates averaged crystallite size (L) to the Scherrer constant (k , here: 0.9), wavelength (λ), full peak width at half maximum (B , in *unit rad*) and scattering angle (θ). The averaged crystallite size refers to individual crystals or regions of coherent crystalline structure, and is not to be confused with particle size. B was corrected for instrumental peak broadening (B_i) of the measured sample peak width (B_s) by comparison with a standard material (CeO₂),

$$B^2 = B_s^2 - B_i^2 \quad (2)$$

We used the highest intensity hematite (1 0 4) peak for L parameter analysis from both PXRD and SRXRD patterns.

4. Results

4.1. Petrography

The M-mplH ore usually has a banded texture defined by discrete hematite micro- and mesobands, which can be strongly folded and fractured (Fig. 2a and b). Petrographic observation reveals abundant, randomly oriented hematite microplates that occupy the space between the microbands (Fig. 2c). The microplates can reach sizes from 1 μ m to several 100 μ m and they are associated with large pore spaces, depending on their size and density, which contrasts with hematite bands that are commonly less porous (Fig. 2c–f). However, it is usually difficult to delineate pre-existing sedimentary/diagenetic microbands from newly formed bands of microplaty hematite due to wide variation in grain sizes, habits and the extent of hematite intergrowth (Fig. 2a and b). The upper and lower boundaries of the hematite bands are frequently jagged and irregular, which is accentuated by intergrowth with microplaty hematite (Fig. 2c–e). No detectable intragranular textural or compositional changes of either hematite bands or microplates are observed in reflected plane polarised light (RPPL) (Fig. 2c).

Reflected crossed polarised light microscopy (RXPL) reveals that hematite bands have a complex texture that is dominated by μ m-sized anhedral crystals with inequigranular to seriate grain size distributions, and interlobate to amoeboid grain boundaries (Fig. 2d–f). In contrast, microplates are commonly euhedral and usually do not display intragranular (sub-) textures in RXPL (Fig. 2e). Both, anhedral hematite and microplaty hematite show no preferred orientation in our samples (Fig. 2e, f). The porosity of the M-mplH is frequently partly or completely filled with a very fine-grained matrix with a dull brown to grey reflectance colour in RPPL and strong orange to red internal reflections in RXPL, which is characteristic for hematite (Fig. 2e).

The discovery of relict BIF in microplaty hematite ore has enabled us to study the lateral transformation of chert containing abundant hematite colloids into hematite ore (Fig. 3a and b). The banding of the ore is parallel to chert bands of the BIF remnant, indicating that the latter has formed *in situ* from a chert-rich progenitor (Fig. 3a and b). The dark brown colour of the chert bands derives from abundant inclusions of hematite. The remnants of the chert bands are crosscut by quartz veins that do not extend into the massive bands of hematite suggesting that veining in this sample occurred prior to ore genesis (Fig. 3a and b). The chert from the relict BIF is surrounded vertically (Fig. 3c and d) and laterally (Fig. 3e and f) by large amounts of hematite particles (~100 nm–5 μ m), which can be identified by their characteristic weak red internal reflections in RPPL (Fig. 3c and d). However, RXPL reveals strong internal reflections of orange and red (Figs. 2e, 3e, f). This unexpected colour range is caused by the size or shape of the hematite particles, with smaller particles causing a shift in the reflective colour of hematite towards orange (Cornell and Schwertmann, 2003; Köhler and Kischkewitz, 2014). This interpretation is supported by PXRD analyses of both the relict chert and juxtaposed iron oxide minerals, which confirm the presence of hematite (Table 1: ME13/14). Low abundances of goethite indicate that weathering has not significantly affected the analysed samples. The matrix of fine-grained hematite predominately fills the space between hematite microbands that is occupied microplaty

The larger hematite microplates are randomly embedded inside the hematite particle matrix and do not nucleate on the BIF remnant (Fig. 3c and d). We have not found any evidence for microplaty hematite transport within the porosity that links nearby hematite bands or within the matrix of hematite particles. A similar evaluation of the scale on which hematite particle transport occurs is difficult due to their high abundance, their small grain size and the large volume of available porosity. However, we assume that transport distances were probably short as similar particles are present as inclusions within the adjacent chert relict and could have acted as a source for microplaty hematite (Fig. 3b–d). Moving laterally away from the BIF remnant into the M-mplH ore, the compactness and apparent grain size of microplaty hematite increase together with the development of strong mutual intergrowth of microplaty hematite. Further intergrowth results in progressively denser networks of microplaty hematite that transgress into anhedral hematite microbands accompanied by grain size reduction, loss of microplaty habit and a decrease in porosity (Fig. 3c, f, i, j).

Hematite particles are not only restricted to the vicinity of the BIF remnant but is also located in most pore spaces, especially larger pores located between individual microbands (Fig. 3g and h). The irregular boundaries of hematite bands are usually associated with an inward decrease in grain size to the centre of the band, with a transition from microplaty to fine-grained anhedral hematite as outlined above (Fig. 3h). Our textural observations of the transition from hematite particles, and microplaty hematite to 'mosaic' hematite exclude precipitation of microplaty hematite between hematite bands from solution in a similar fashion to vein minerals with comb structures or layered mineral precipitates. This is because microplates are typically not in contact with hematite bands and do not produce a fabric.

Besides the ubiquity of euhedral microplaty grains, other larger euhedral to subhedral, hematite grains with rhombohedral or

Table 1
PXRD analysis results.

					Coordinates			Composition								Crystallite Size				
	Sample	ID	Location	Lithology	Easting	Northing	Elevation	Hem	Goe	Qtz	Mgt	Pyr	Kao	Ccp	AP	Total	Rp	L (Hem)	L (Goe)	
BIF	ME13/2a	1	B26	DG	n/a			14.1		85.4			0.5			100	7.7	146.2		
		2						15.5		81.3			3.2			100	9.2	149.6		
	ME13/16	1	MTP	DG	n/a			11.5	0.2	88.3					100	7.6	100.7			
		2						49.8	0.5	49.7					100	6.0	151.1			
		3						50.6	0.4	49					100	5.6	148.6			
	ME13/22	1	MTP	JOF	577570	7482522	1035	10		90					100	7.7	11.41			
		2						10.2		89.8					100	9.3	94.5			
	ME14/5	1	MT	DG	541972	7489549	699													
	ME14/9b	1	MT	DG	542690	7490171	733	2.7		97.3						100	14.3	78.8		
		2						40	17.7	42.3					100	9	50.3	85.1		
Iron ore	ME13/8*	AB	MTP	DG	579720	7481850	630	100								100	10.7	105		
		1						99.5		0.5					100	9.8	120.7			
	ME13/14*	1	MTP	DG	579354	7482006	629	59.9	2.9	37			0.2		100	6.3	150.8			
		2						94.2	3.1	1.4				1.3		100	9.5	90.1		
		B						97.9	2.1						100	9.2	87			
		D						100							100	9.4	105.5			
	ME14/1	A	MT	DG	541779	7489389	640	100								100	8.3	67.6		
		B						100							100	7.9	65.1			
		C						100							100	8.8	57.2			
	ME14/3	1	MT	DG	541776	7489523	655													
	ME14/23	A	MT	MM	542509	7488586	637	74.2	3.2	0	5.9	16.7				100	8.6	47.1		
		B						62.1			10	25.6			2.3	100	11.9	46.5		
		C						54.8	6.7		5.3	32.3	0.9			100	11.8	46.8		
	ME14/28a*	A	MTP	DG	579720	7481850	629	100								100	9	131.6		
	ME14/28b*	AB	MTP	DG				100									100	9.3	88.4	
		C						100								100	9.6	106.5		

approximate coordinates as samples are not *in situ* due to mining activities (coordinates in WGS84, Zone: 50 K)

ID (numbers) subsamples analysed at Monash University.

ID (letters) subsamples analysed at Max-Planck Institute of Colloids and Interfaces.

L Crystallite size – Scherrer.

Rp profile R-factor.

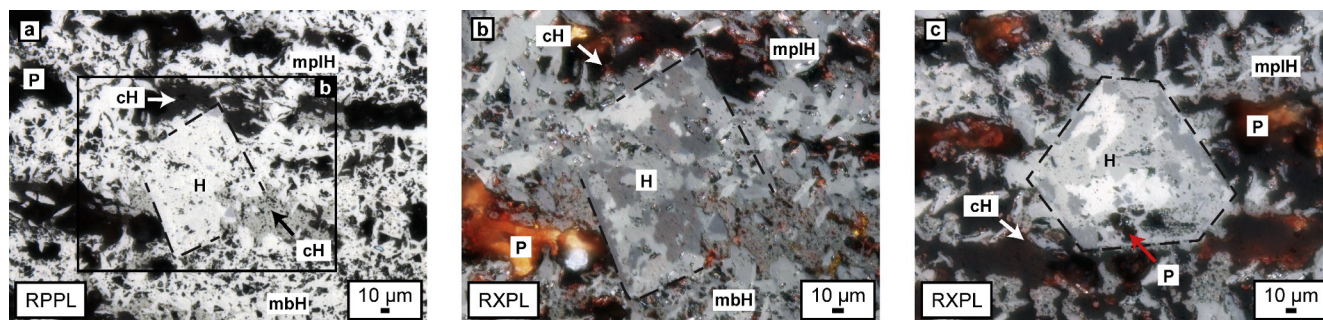


Fig. 4. Euhedral hematite minerals in M-mplH ore. a) Straight crystal faces of hematite indicate euhedral to subhedral crystals in hematite microbands. These crystals are intergrown with the adjacent hematite microbands, microplaty hematite, surrounding hematite particles and provide some microporosity. b) Inset of (a) under RXPL showing that euhedral to subhedral rhombohedral crystals are composed of a complex irregular texture of multiple anhedronal hematite crystals with intergranular porosity similar to textures of hematite microbands (e.g., Fig. 2f, 3j). c) Similar observations to those in (b) but with hexagonal habit of the ‘pseudo-single’ crystal. H: hematite, mbH: microbanded hematite, mplH: microplaty hematite, cH: colloidal hematite/hematite particles, P: porosity, RPPL: reflected plane polarized light, RXPL: reflected crossed polarized light.

hexagonal habits are common (Fig. 4a and c). Internal textures were not visible in these grains under RPPL but significant intragranular porosity and diffuse crystal boundaries are visible due to intergrowth with microplaty hematite, anhedronal hematite or hematite particles (Fig. 4a). RXPL revealed a complex anhedronal pattern of seriate and interlobate hematite crystals (Fig. 4b and c) similar to textures previously observed in hematite microbands (Fig. 2f; 3f, h, j). The intragranular texture does not show zonation related to sequential crystal growth and porosity is predominantly located at grain boundaries between anhedronal hematite crystals. Euhedral hematite crystals are commonly interpreted to be a pseudomorphic replacement of magnetite (i.e., martite) by hematite (Morris, 2012, 1985); however, it is not known whether these ‘pseudo-single’ crystals can form by assembling smaller hematite grains or

particles (Fig. 4).

4.2. SEM and TEM

We further investigated the relationship between hematite particles and microplaty hematite by SEM, focussing on areas of higher porosity filled with hematite particles (Figs. 5 and 6). Our analysis revealed a range of hematite minerals varying in size and shape. Large, euhedral, microplaty hematite crystals (mplH₁), equivalent to the microplaty hematite shown previously (Fig. 3) range from several µm to hundreds of nm in size (Fig. 5a, c, e). These larger mplH₁ crystals can comprise smaller euhedral hematite microplates (mplH₂) ranging in size from several hundreds of nm to 1 µm (Fig. 5a and b). The degree of preferred

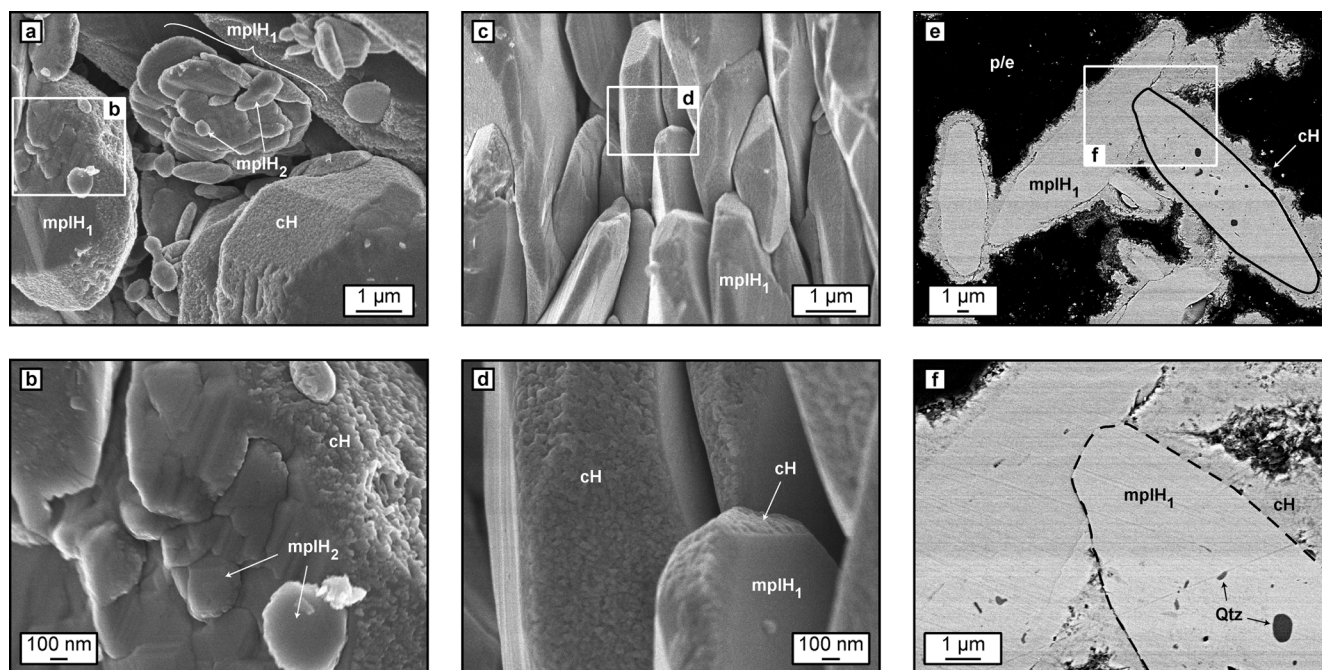


Fig. 5. SEM images of microplaty hematite crystals in M-mplH ore. a, b) Secondary electron (SE) image of microplaty hematite (mplH₁) comprising smaller hematite platelets (mplH₂). Lateral surfaces of mplH₁ and mplH₂ are coated with abundant hematite particles (cH), whereas circular bases show smooth, particle-free faces (c, d). e, f) Backscattered electron (BSE) image of porous sample embedded with epoxy (p/e) showing mplH₁ crystals surrounded by a μm-thick layer of cH and spherical quartz (Qtz) inclusions in mplH₁.

orientation and interconnection between individual mplH₂ crystals varies from loose stacking (Fig. 5a: centre) to dense aggregates of hematite platelets with faint grain boundaries and strong mutual intergrowth (Fig. 5b). Both mplH₁ and mplH₂ crystals show different degrees of surface roughness on different crystal faces, with smooth surfaces on circular bases and irregular relief on lateral faces (Fig. 5b and d). The relief stems from abundant randomly shaped hematite particles ranging in size from 10 to 200 nm, which are attached to lateral crystal faces of the microplaty hematite. Coatings of hematite particles in our samples can range in thickness from a single layer of hematite particles (Fig. 5d) to μm-thick layers that cover entire mplH₁ crystals (Fig. 5e and f). It is interesting to note that the presence of spherical quartz inclusions can be seen within mplH₁ crystals in cross section (Fig. 5e and f).

Thicker coatings of hematite particles on mplH₁ crystals illustrate that there is a hierarchy of hematite platelets, whereby larger plates are built from smaller ones (Fig. 6a–d). When viewed at high magnification, it becomes evident that the coatings of hematite particles comprise large quantities of the mplH₂ crystals that have highly irregular surfaces (Fig. 6a and b). The irregularities stem from abundant oriented nanoplaty hematite (nplH) crystals that build up the larger mplH₂ crystals (Fig. 6c and d). Cross sections of mplH₁ crystals and their coatings can show a reduction of porosity and fusion of the particles towards the mplH₁ interface (Fig. 6e–g). Areas where the thick coatings are removed expose direct crystal faces of mplH₁, which are speckled with nm-sized particles (Fig. 6h) similar to aforementioned thin hematite particle coatings (Fig. 5b and d).

TEM analyses of nplH coatings on mplH₂ crystals reveal more details about nplH crystals (Fig. 7). The mplH₂ crystals have highly irregular crystal faces as a result of the commonly (sub-) parallel alignment of nplH crystals from which they are constructed (Fig. 7a and b). Individual mplH₂ crystals are commonly oriented at ~60° to neighbouring mplH₂ crystals as a result of the hexagonal crystal structure of hematite (Fig. 7b). Our observations highlight that mplH₂ are not single crystals but represent aggregates of imperfectly attached, crystallographically aligned nplH. High-resolution TEM reveals that the

atomic-scale interfaces between individual nplH crystals are indeed (sub-) parallel. Fast Fourier Transformations (FFT) of adjacent nplH crystals demonstrate that adjacent nplH have similar, but typically imperfect, crystallographic orientations (Fig. 7d).

4.3. XRD

We quantified the distribution of hematite particles at different scales in BIF and BID samples using PXRD and SRXRD. Our PXRD study reveals that most BIF samples are composed of mainly hematite and quartz with minor amounts of goethite (Table 1, Fig. 8). Chert bands are characterised by high concentrations of quartz (> 80 wt%) and 10–15 wt% of hematite colloids, whereas BIF hematite bands show substantial quartz content (~50 wt%) and higher hematite concentrations (40–50 wt%). M-mplH samples commonly comprise large quantities of hematite (up to 100 wt%) and only low abundances of quartz (< 2 wt%) apart from samples containing chert relicts (e.g., Table 1: ME13/14–1). The M-mplH samples can also contain magnetite, pyrolytite and chalcopyrite.

Analyses of hematite (1 0 4) diffraction peaks show peak broadening effects related to small crystallite sizes in all powdered samples (e.g., Fig. 8). Crystallite size analysis using Scherrer's formula resulted in hematite crystallite sizes ranging from 40 to 150 nm for both, BIF and M-mplH ore (Table 1). This analysis shows that hematite nanocrystallites are abundant in BIF and iron ore. Although there are some variations in crystallite sizes between different layers (different sub-samples), we cannot detect any trends from the data set (Table 1).

We conducted SRXRD, a technique that is commonly used in the field of biomaterials (e.g., Paris, 2008), to identify the *in situ* spatial distribution of hematite nanocrystallites in BIF and iron ore samples (Fig. 9, Appendix). All our analysed samples show widespread occurrences of hematite nanocrystallites (Fig. 9c, h, i, Appendix), suggesting that small hematite crystallite sizes are pervasive in both BIF and iron ore, which has not been identified previously. Microbands of anhedral hematite in BIF commonly show crystallite sizes between 110 and 140 nm (Fig. 9c). Larger euhedral hematite crystals reveal smaller

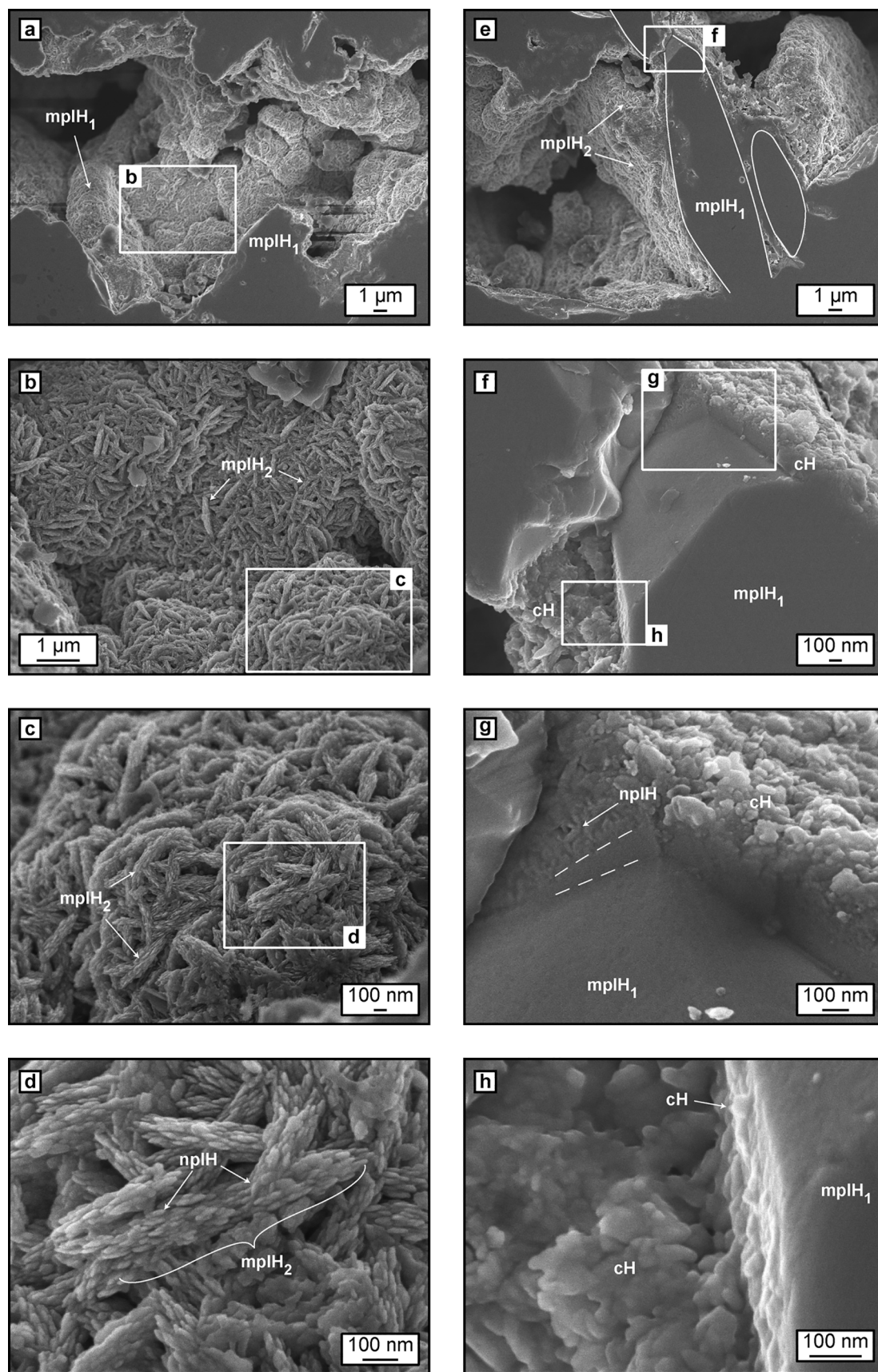


Fig. 6. SE images of microplaty hematite crystals in M-mplH ore. a, b) mplH₁ crystals are coated with smaller randomly oriented mplH₂ minerals. c, d) High-resolution images reveal that mplH₂ crystals comprise smaller nanoplaty hematite (nplH) crystals. e, f) mplH₁ crystals coated with mplH₂ and cH. g) cross-section of mplH₁ crystal and cH coating showing a densification (between dashed lines) of the coating particles (cH and nplH) towards the mplH₁ surface. h) High-resolution image of the mplH₁ surface showing cH attached to the mplH₁ surface similar to Fig. 5b, d.

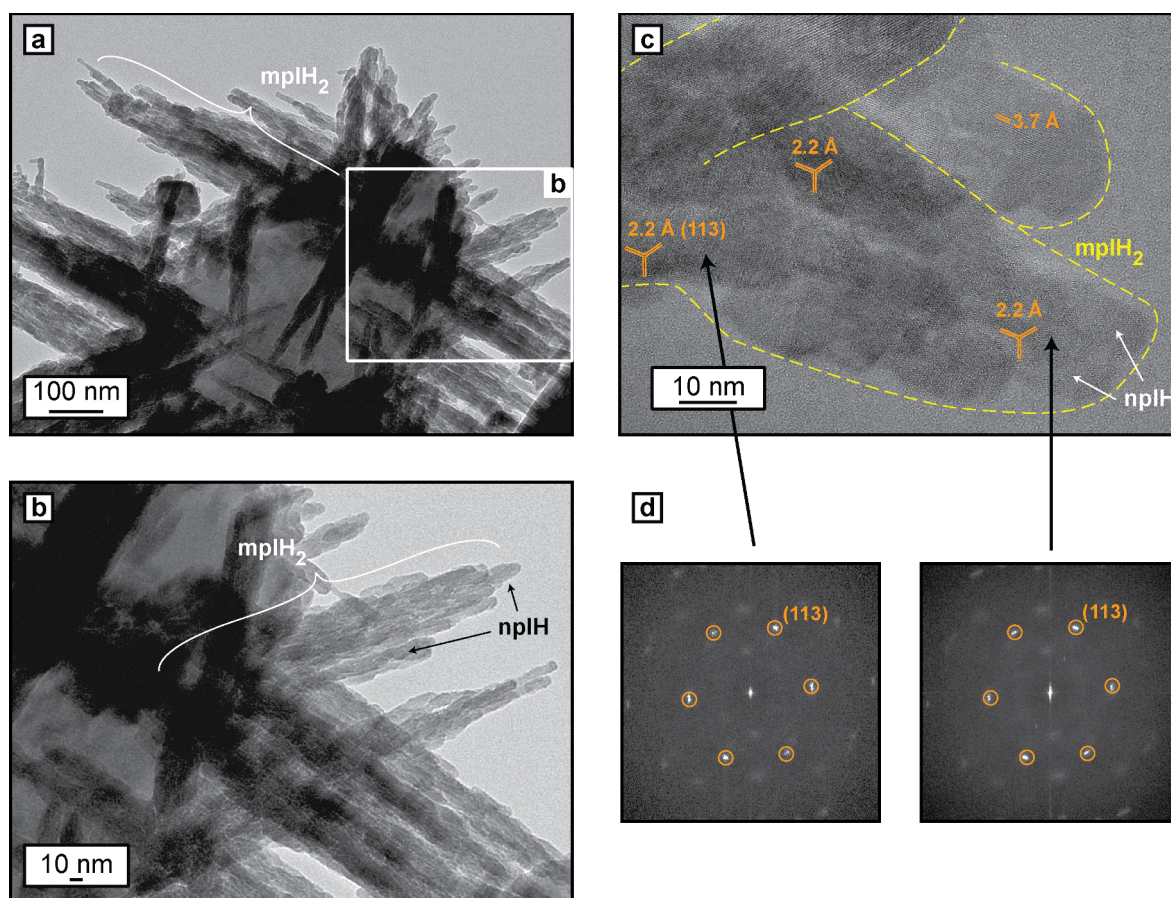


Fig. 7. TEM images of microplaty hematite crystals (mplH₂). a, b) MplH₂ crystals (yellow dashed line) comprise many crystallographically aligned nanoplath hematite crystals (nplH). Different mplH₂ are regularly oriented at ~ 60° to each other. c) High resolution TEM image showing the nanoplath texture of mplH₂. Atomic interfaces (orange) of adjacent nplH crystals align. d) Fast Fourier Transformations showing bright hexagonal maxima corresponding to hematite (1 1 3) and weak spots likely correspond to hidden/small hematite crystal of different orientation.

crystallite sizes ranging from 20 to 70 nm (Fig. 9c). Jasper bands hosting abundant encapsulated hematite colloids commonly do not contain hematite at sufficient abundance to provide the peak intensity needed for crystallite size analysis. However, previous studies (e.g., Rasmussen et al., 2015; Sun et al., 2015) and our PXRD analyses (Table 1) have demonstrated the presence of hematite particles in chert bands. Hematite microbands of M-mplH ore show slightly smaller crystallite sizes (80–120 nm) than layers dominated by microplaty hematite (100–140 nm).

The diffraction patterns of individual spots (boxes: Fig. 9c, h, l) give more information about the relationship between crystallite sizes obtained from PXRD and SRXRD analyses and crystal/grain sizes observed in our petrographic study (Figs. 3, 4, 9). Faint, diffuse and complete rings in diffraction patterns represent random orientations of crystallites (Fig. 9d, e), whereas sharp, intense points and streaks represent preferred orientations of crystallites (Fig. 9i, j). Streaks indicate that many hematite crystallites have similar orientations but not the identical orientation whereas a single crystal of hematite will give sharp, discrete small point maxima [e.g., Hematite (1 0 4): Fig. 9d, e, i, j]. Hence, our petrography and diffraction analysis shows that the majority of larger, μm-sized hematite grains in our samples are composed of smaller nm-sized hematite crystals.

5. Discussion

The presence of nanocrystalline hematite in M-mplH ore has not been recognised previously. We have presented evidence that both hematite microbands and microplaty hematite crystals are built by

aggregation of nm-sized hematite particles. Our direct observations of the transition from colloid-rich chert bands to microplaty hematite, and ultimately to mm-scale hematite microbands (Fig. 3) does not support precipitation from iron-rich solutions or, metamorphic replacement of either goethite (Morris, 2003, 1985, 1980; Morris and Kneeshaw, 2011) or iron-bearing carbonate minerals (Taylor et al., 2001; Thorne et al., 2014, 2004) by hematite. This discovery leads to new perspectives in understanding M-mplH ore genesis.

Instead, we suggest that quartz dissolution during ore genesis led to liberation of colloidal hematite inclusions from chert bands, which aggregated *in situ* and formed new microplaty hematite crystals, eventually building new layers of microplaty hematite that mimic the original banded texture of BIFs (Fig. 3). These hematite microplates subsequently intergrew with pre-existing iron oxide bands instead of nucleating on them from solution, thus leading to the formation of the irregular microband boundaries that we observe (e.g., Fig. 3g and h). Progressive crystallization of microplaty hematite and fusion of microplaty aggregates led to the loss of the microplaty habit and porosity, and its eventual lateral transformation into hematite microbands, which are characterized by irregular anhedral textures (Fig. 3j). There is compelling evidence provided by geochemical studies for the presence of hydrothermal saline fluids in many iron ore deposits of the Hamersley Province (Barley et al., 1999; Brown et al., 2004; Dalstra et al., 2003; Dalstra, 2014; Taylor et al., 2001; Thorne et al., 2009, 2014, 2006, 2004; Webb et al., 2004). We agree that the infiltration of these hypogene fluids is required for ore genesis as an active quartz dissolution agent that increased quartz solubility by multiple orders of magnitude. This is supported by multiple chemical experiments that

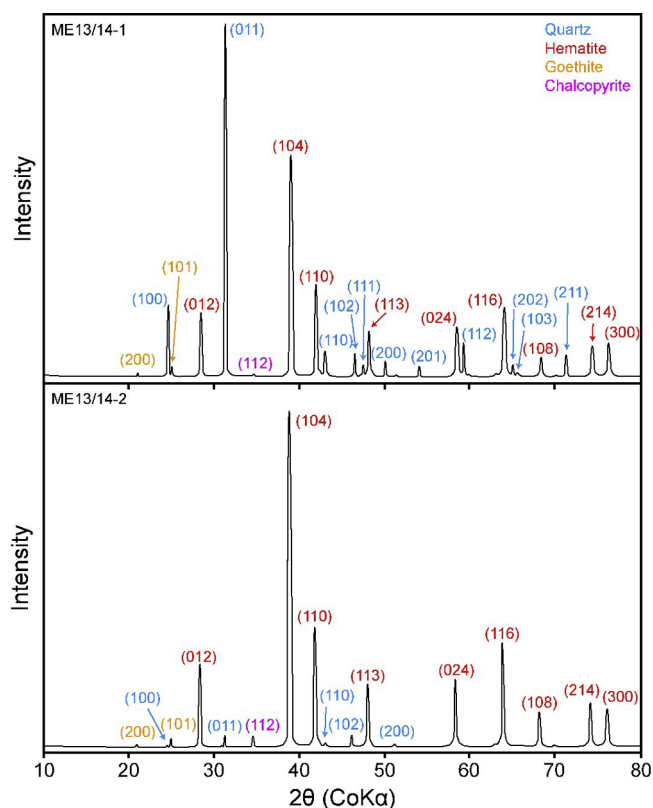


Fig. 8. XRD patterns of BIF (top) and M-mplH ore (bottom).

show an increase of quartz solubility with increasing temperature, salinity and pH (Dove and Elston, 1992; Dove, 1999; Dove and Crerar, 1990; Dove and Nix, 1997). However, it is also important to evaluate the passive role of quartz removal through hypogene fluids on the evolution of iron ore deposits, while placing this within the context of our new observations of non-classical crystallisation during genesis of BIDs.

5.1. Particle-based crystallisation in M-mplH ore

Previous studies have suggested that microplaty hematite forms from goethite by metamorphic recrystallisation (Morris, 1985) or by replacement of iron carbonates (Taylor et al., 2001). These concepts are based on classical crystallisation pathways (e.g., Ostwald ripening, dissolution–precipitation), which require the dissolution of the hematite particles in a suitable fluid and instantaneous precipitation of the dissolved ions onto an existing nucleus (Cölfen and Antonietti, 2008). Larger crystals would then grow at the expense of smaller crystals and eventually lead to euhedral, defect-free and void-free crystals with smooth faces (Fang et al., 2011).

However our SEM and TEM studies reveal a self-similar hierarchy of smaller hematite crystals building larger hematite crystals on the scale of nanometres to micrometres (Figs. 5 and 6). In combination with our XRD data we have shown that microplaty hematite (mplH₁) are not perfectly single-crystalline because they consist of smaller hematite platelets (mplH₂) and hematite particles (ch) creating rough lateral surfaces but not on the circular base. A perfect single crystal would have smooth faces instead. Further, we have demonstrated that hematite particles are neither localised nor rare, but are ubiquitous in both BIF and iron ore samples (Table 1, Fig. 9). These observations are not in accordance with classical crystallisation theory, which suggests that nanoparticulate phases should have been consumed during hydrothermal alteration. Instead, we propose that large euhedral hematite crystals (e.g., microplaty hematite) and anhedral massive bands of

hematite in our BIF and iron ore samples formed predominantly from existing hematite colloids that were released during removal of chert from the system.

Attachment can occur by coalescence of particles after collision with mutual crystallographic orientations, by particle rotation or imperfect oriented attachment (e.g., Cölfen and Antonietti, 2008; Leite and Ribeiro, 2012; Madden et al., 2010; Zhang et al., 2010). Nevertheless, there are many formation and transformation pathways (both classical and non-classical) taken by iron hydroxides, iron oxyhydroxides and iron oxides (Cornell and Schwertmann, 2003; Faivre, 2016; Guo and Barnard, 2013). Complex combinations of oriented attachment, dehydration/hydration reactions and recrystallization by Ostwald ripening lead to a wide range of crystal shapes controlled by the precursor species and the prevailing fluid conditions (e.g., Cornell and Schwertmann, 2003; Guo and Barnard, 2013; Patra et al., 2016). Recognising that iron ore deposits and BIF form by such complex combinations of classical and non-classical crystallisation pathways is important in that it provides a framework for understanding the genetic history of these deposits in greater detail.

5.2. Passive fluid effects on particle transport

From our observations, new questions arise about the controlling factors of hematite particle transport and their attachment. The behaviour of colloids in suspension is strongly controlled by physicochemical interactions between the particles, the fluid in which they are suspended, and the nature of the porous medium through which the particles and fluid travel. Interactions among the particles, fluid and the pore network lead to dynamic particle deposition and release phenomena (Chen and Flury, 2005; Kuznar and Elimelech, 2007; Tosco et al., 2012). Most studies on colloidal suspensions show that the processes of flocculation, coagulation and deposition of suspended particles are enhanced with increasing ionic strength, which affects the electric surface potential of particles. In contrast, low ionic strength solutions, in particular those with high pH values, lead to increased mobilisation of nanoparticles (Israelachvili, 2011; Ko and Elimelech, 2000; Kuznar and Elimelech, 2007; McDowell-Boyer, 1992; Ryan and Elimelech, 1996; Saleh et al., 2008; Tosco et al., 2012, 2009). Saline fluids therefore significantly limit particle transport distances and lead to proximal deposition of particles, such as the hematite colloids liberated from chert in BIF. The rate of fluid flow also plays a significant role in the distance over which particles may be transported in suspension. For instance, zones of reduced fluid flow velocity, such as stagnation points in porous media, can enhance the rate of particle deposition (Brow et al., 2005; Tong and Johnson, 2006; Tosco et al., 2012). In this context, we assume that the highly-saline hypogene fluids that have been documented in fluid inclusions of metasomatic alteration zones identified in some BIDs (e.g., Taylor et al., 2001) had a critical impact on hematite particles derived from BIF leading to short transport distances, enhanced attachment and aggregation. This can explain why BIDs are residual deposits and iron is commonly not removed from the system or relocated and reprecipitated in neighbouring rock formations.

5.3. Application to M-mplH ore genesis

The importance of hypogene and supergene fluids in the formation of M-mplH deposits has been highlighted before (e.g., Taylor et al., 2001), but it has not been demonstrated geochemically or experimentally how microplaty hematite could have formed from these solutions. Many studies agree that the host BIF contains enough iron to account for the production of microplaty hematite (e.g., Taylor et al., 2001), but the exact source of iron and the mechanism by which the final ore is produced has been enigmatic. Specifically, it had previously been assumed that the ‘secondary’ iron required for the formation of microplaty hematite must have been dissolved; the iron species is unknown

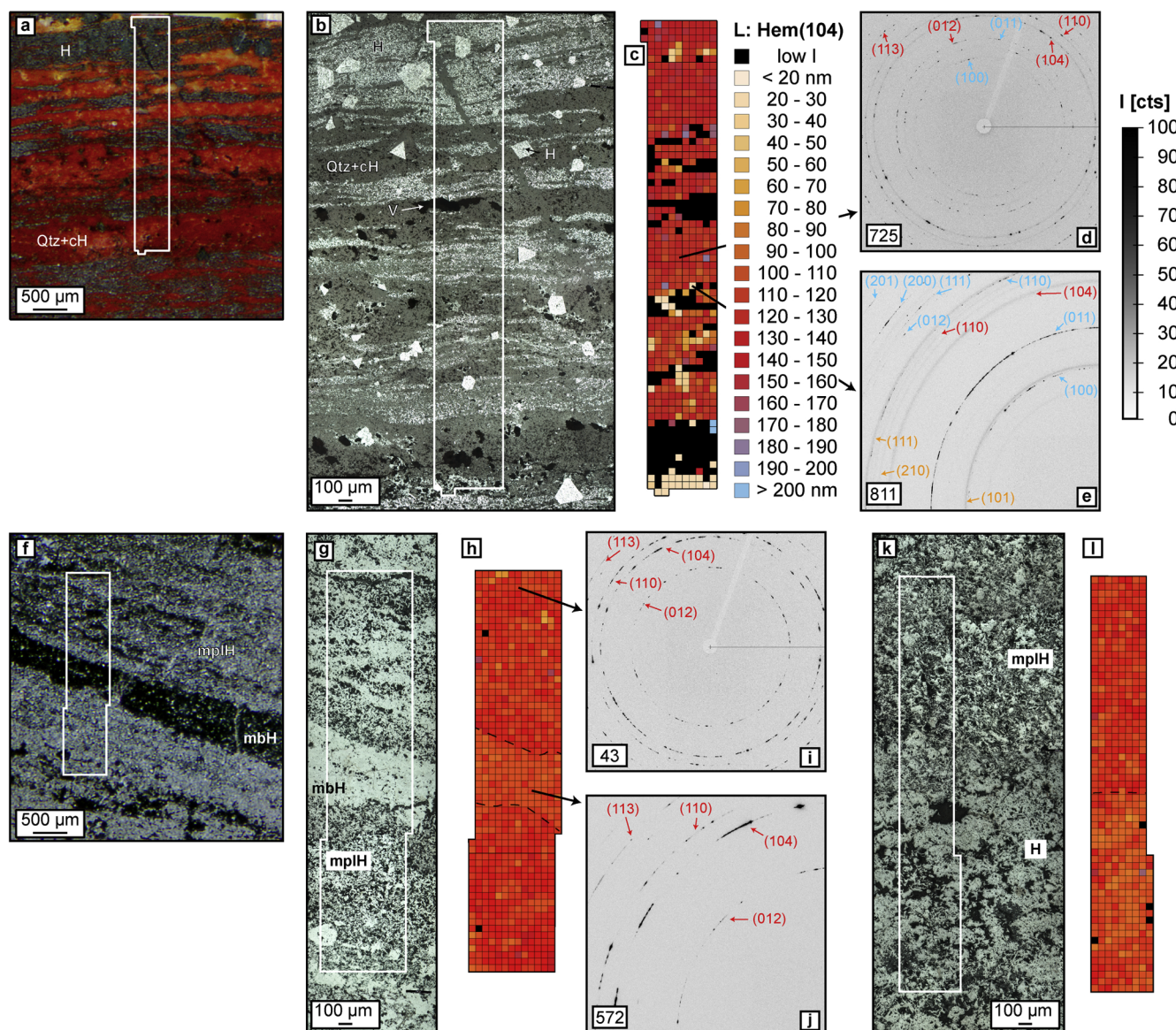


Fig. 9. SRXRD analyses of BIF and M-mplH ore. Thin section scans (a, f), RPPL images (b, g, k), crystallite size maps (c, h, l) with color code (c), and XRD patterns of samples ME14/5 (a–e), ME13/8 (f–j) and ME14/28b (k, l). Hematite crystallite sizes smaller than 200 nm are widespread in our samples and show local, layer-dependent variations (c, h, l). Large euhedral hematite crystals in BIF reveal smaller hematite crystallite sizes in relation to hematite microbands (a–c). Coarser grained hematite microbands (mbH) in M-mplH ore show smaller crystallite sizes than adjacent microplaty hematite layers (g, h, k, l). Diffraction patterns show diffraction of specific faces of hematite (red), quartz (blue) and goethite (orange) (d, e, i, j) at different locations (e.g., 725). Faint rings represent abundant unoriented crystals (e), streaks show similar orientations of many crystals (e, j), point maxima represent single crystals or equal orientation of many crystals. Resolution (box size): 50x50 μm. Note: black boxes (c, h, l) do not necessarily represent hematite-free areas, only very low intensities with lower quality crystallite size results. I: intensity [cts: counts], L: crystallite size, Hem, H: hematite.

(Taylor et al., 2001; Thorne et al., 2014). Direct precipitation of microplaty hematite from a solution or replacement of precursor iron carbonates or magnetite requires fluids supersaturated in iron. However, we have not identified leaching of any iron oxide minerals in BIF or textures that suggest precipitation of ‘secondary’ iron oxide minerals in our BIF samples.

Taylor et al. (2001) attempted to calculate the mass balance of the upgrading of BIF to iron ore in the Hamersley Province. They determined that iron ore genesis at the Mount Tom Price deposit was accompanied by a stratigraphic thinning of ~40 vol% in relation to the BIF precursor. Furthermore, microplaty hematite ore shows high porosities up to 30 vol% resulting in a total loss of 55–60 vol% of the BIF precursor. This means that iron oxides in the BIF contributed only

40–45 vol% to the final ore body (Taylor et al., 2001). Our petrographic observations suggest that iron for microplaty hematite crystallisation was derived from encapsulated hematite particles in quartz grains. Chert bands contain around 10 vol% of hematite particles, however their concentration can vary substantially (Rasmussen et al., 2015). Bulk chemical analyses of BIF bands show that BIFs contain about 50 wt % iron oxides, 45 wt% SiO₂ and 5 wt% minor phases [data from Taylor et al., (2001): drillhole RC96B26E001]. Based on these numbers we present a rough estimation to evaluate the amount of microplaty hematite that can form from encapsulated hematite particles in relation to the bulk ore.

We assume for our calculation that all silica is bound in quartz and we ignore all phases other than iron and silica phases. We therefore

estimate that BIF contains 35 vol% iron oxides and 65 vol% quartz. Quartz hosts ~10 vol% of hematite particles (Rasmussen et al., 2015) increasing the volume of chert including hematite particles to 75 vol% and decreasing the volume of pre-existing iron oxide bands to 25 vol% of the BIF precursor. Consequently, ~30 vol% of all iron oxides in BIF are represented by hematite particles and ~70 vol% by pre-existing iron oxide bands. Quartz removal from the BIF during ore genesis results in iron ore comprising 70 vol% iron oxides and 30 vol% porosity. Breaking down the iron oxide concentration in iron ore into hematite particles released from chert and pre-existing iron oxide bands we obtain a contribution of hematite particles to iron ore of 20 vol% and 50 vol% for iron oxide bands at a given porosity of 30 vol%.

This rough estimate suggests that an initial hematite particle concentration in chert bands of 10 vol% could account for 20 vol% of microplaty hematite in the final ore. Initial concentrations of 5 vol% or 20 vol% result in an iron oxide contribution of hematite particles to the final ore of 10 vol% or 40 vol% respectively. Our calculations are supported by unpublished reconnaissance data obtained by RioTinto Ltd., which showed that the concentration of microplaty hematite in different types of M-mplH ore at the Mount Tom Price deposit ranges from 10% to 55% at an average of 32.7% (sample size: 17). We have shown that hematite particles are a realistic iron source for microplaty hematite and that addition of iron from external sources is not required to form M-mplH ore. Nevertheless, we consider that our evaluation supports the significance of quartz removal as the major iron ore-forming process. Based on our observations, we consider that warm, highly saline fluids would have increased the solubility of quartz and enhanced the attachment efficiency of the particles, resulting in higher rates of flocculation and aggregation, leading to shorter travel distances and more efficient deposition (e.g., Tosco et al., 2012). This phenomenon may explain why very large M-mplH ore bodies are commonly located close to the infiltration point of the exotic fluids into BIF, such as faults. Crystallisation by particle attachment does not require fluids supersaturated in dissolved carbonate or iron, and does not need corresponding metasomatic alteration zones. Hence, we agree that carbonate alteration zones are probably linked to microplaty hematite formation as suggested before (e.g., Taylor et al., 2001), but they are not a prerequisite to form M-mplH ore bodies and rather represent localities of extreme fluid conditions.

6. Conclusions

Our findings reveal that large crystals of hematite within M-mplH ore minerals are built up by aggregation of abundant nanoscale hematite particles. These hematite particles originated from abundant hematite inclusions that were originally present within chert bands in the host BIF. Colloidal inclusions of hematite were liberated upon quartz dissolution, which was facilitated by the infiltration of warm, highly saline aqueous solutions, but the fate of dissolved quartz remains unknown. Subsequently, these saline fluids enhanced the aggregation and proximal deposition of hematite particles that aggregated and attached to form larger microplaty hematite crystals via non-classical crystallisation pathways. Progressive oriented attachment of hematite particles led to fusion of the microplates and transformation into hematite micro- and mesobands to form pure, porous hematite ore.

Acknowledgements

We are grateful to Leigh Nicholas and Jim Gordon and their teams as well as many other geologists at RioTinto Iron Ore Ltd. and RioTinto Exploration Ltd. for their abundant and helpful support. M.S.E. is thankful for a Bicentennial Gold 88 award (AusIMM). M.S.E. and A.R.C. also acknowledge Monash University for scholarship and research

support, respectively. Research in D.F. lab is supported by the Max Planck Society. We thank Nathan Webster, CSIRO Mineral Resources, Australia, for his generous help with collecting XRD patterns. We also thank many colleagues at Monash University, Australia (Marianne Richter: SEM; Tim Williams: TEM) and the MPIKG, Germany for their help with data acquisition and analysis (Ingo Schmitt: DPDAK, Ingrid Zenke: SRXRD, PXRD; Heike Runge, Tobias Weil and Lucas Kuhrts: SEM, TEM). Special thanks to Junnel Alegado (Monash University, Australia) and Christine Fischer (University of Potsdam, Germany) for their sample preparation efforts. We are grateful to Bruce Simonson, Paul Duuring and an anonymous reviewer for their helpful comments.

Appendix A. Supplementary data

Supplementary data to this article can be found online at <https://doi.org/10.1016/j.oregeorev.2018.10.001>.

References

- Barley, M.E., Pickard, A.L., Hagemann, S.G., Folkert, S.L., 1999. Hydrothermal origin for the 2 billion year old Mount Tom Price giant iron ore deposit, Hamersley Province, Western Australia. *Miner. Depos.* 34, 784–789. <https://doi.org/10.1007/s001260050238>.
- Baumgartner, J., Faivre, D., 2015. Iron solubility, colloids and their impact on iron (oxyhydr)oxide formation from solution. *Earth Sci. Rev.* 150, 520–530. <https://doi.org/10.1016/j.earscirev.2015.09.003>.
- Bekker, A., Slack, J.F., Planavsky, N., Krapež, B., Hofmann, A., Konhauser, K.O., Rouxel, O.J., 2010. Iron formation: The sedimentary product of a complex interplay among mantle, tectonic, oceanic, and biospheric processes. *Econ. Geol.* 105, 467–508. <https://doi.org/10.2113/gsecongeo.105.3.467>.
- Benecke, G., Wagermaier, W., Li, C., Schwartzkopf, M., Flucke, G., Hoerth, R., Zizak, I., Burghammer, M., Metwalli, E., Müller-Buschbaum, P., Trebbin, M., Förster, S., Paris, O., Roth, S.V., Fratzl, P., 2014. A customizable software for fast reduction and analysis of large X-ray scattering data sets: applications of the new DPDAK package to small-angle X-ray scattering and grazing-incidence small-angle X-ray scattering. *J. Appl. Crystallogr.* 47, 1797–1803. <https://doi.org/10.1107/S1600576714019773>.
- Bish, D.L., Howard, S.A., 1988. Quantitative phase analysis using the Rietveld method. *J. Appl. Crystallogr.* 21, 86–91. <https://doi.org/10.1107/S0021889887009415>.
- Brow, C.N., Li, X., Ricka, J., Johnson, W.P., 2005. Comparison of microsphere deposition in porous media versus simple shear systems. *Colloids Surf., A* 253, 125–136. <https://doi.org/10.1016/j.colsurfa.2004.11.005>.
- Brown, M.C., Oliver, N.H.S., Dickens, G.R., 2004. Veins and hydrothermal fluid flow in the Mt. Whaleback Iron Ore District, eastern Hamersley Province, Western Australia. *Precamb. Res.* 128, 441–474. <https://doi.org/10.1016/j.precamres.2003.09.013>.
- Burton, W.K., Cabrera, N., Frank, F.C., 1951. The growth of crystals and the equilibrium structure of their surfaces. *Philosoph. Trans. R. Soc. A: Mathemat. Phys. Eng. Sci.* 243, 299–358. <https://doi.org/10.1098/rsta.1951.0006>.
- Cheary, R.W., Coelho, A., 1992. Fundamental parameters approach to x-ray line-profile fitting. *J. Appl. Crystallogr.* 25, 109–121. <https://doi.org/10.1107/S0021889891010804>.
- Chen, G., Flury, M., 2005. Retention of mineral colloids in unsaturated porous media as related to their surface properties. *Colloids Surf., A* 256, 207–216. <https://doi.org/10.1016/j.colsurfa.2005.01.021>.
- Cölfen, H., Antonietti, M., 2008. *Mesocrystals and Non-Classical Crystallization*. John Wiley & Sons, Chichester.
- Cornell, R.M., Schwertmann, U., 2003. *The Iron Oxides*, 2nd ed. Wiley-VCH, Weinheim.
- Dalstra, H., Guedes, S., 2004. Giant hydrothermal hematite deposits with Mg-Fe metasomatism: a comparison of the Carajas, Hamersley, and other iron ores. *Econ. Geol.* 99, 1793–1800. <https://doi.org/10.2113/gsecongeo.99.8.1793>.
- Dalstra, H., Harding, T., Riggs, T., Taylor, D., 2003. Banded iron formation hosted high-grade hematite deposits, a coherent group? *Appl. Earth Sci. (Trans. Inst. Min. Metall. B)* 112, 68–72. <https://doi.org/10.1179/0371745032250111>.
- Dalstra, H.J., 2014. Structural evolution of the Mount Wall region in the Hamersley province, Western Australia and its control on hydrothermal alteration and formation of high-grade iron deposits. *J. Struct. Geol.* 67, 268–292. <https://doi.org/10.1016/j.jsg.2014.03.005>.
- Dalstra, H.J., 2006. Structural controls of bedded iron ore in the Hamersley Province, Western Australia – an example from the Paraburdoo Ranges. *Appl. Earth Sci.* 115, 139–145. <https://doi.org/10.1179/174327506X138959>.
- De Yoreo, J.J., Gilbert, P.U.P.A., Sommerdijk, N.A.J.M., Penn, R.L., Whitlam, S., Joester, D., Zhang, H., Rimer, J.D., Navrotsky, A., Banfield, J.F., Wallace, A.F., Michel, F.M., Meldrum, F.C., Cölfen, H., Dove, P.M., 2015. Crystallization by particle attachment in synthetic, biogenic, and geologic environments. *Science* 349, aaa6760. <https://doi.org/10.1126/science.aaa6760>.
- Dove, P., Elston, S., 1992. Dissolution kinetics of quartz in sodium chloride solutions: analysis of existing data and a rate model for 25°C. *Geochim. Cosmochim. Acta* 56,

- 4147–4156.
- Dove, P.M., 1999. The dissolution kinetics of quartz in aqueous mixed cation solutions. *Geochim. Cosmochim. Acta* 63, 3715–3727. <https://doi.org/10.1021/jp0713413>.
- Dove, P.M., Crerar, D.A., 1990. Kinetics of quartz dissolution in electrolyte solutions using a hydrothermal mixed flow reactor. *Geochim. Cosmochim. Acta* 54, 955–969.
- Dove, P.M., Nix, C.J., 1997. The influence of the alkaline earth cations, magnesium, calcium, and barium on the dissolution kinetics of quartz. *Geochim. Cosmochim. Acta* 61, 3329–3340.
- Egglseder, M.S., Cruden, A.R., Dalstra, H.J., Nicholas, L., 2017. The role of deformation in the formation of banded iron formation-hosted high-grade iron ore deposits, Hamersley Province (Australia). *Precamb. Res.* 296, 62–77. <https://doi.org/10.1016/j.precamres.2017.04.034>.
- Egglseder, M.S., Cruden, A.R., Tomkins, A.G., Wilson, C.J.L., 2016. Deformation-induced silica redistribution in banded iron formation, Hamersley Province, Australia. *Lithos* 266–267, 87–97. <https://doi.org/10.1016/j.lithos.2016.09.033>.
- Evans, K.A., McCuaig, T.C., Leach, D., Angerer, T., Hagemann, S.G., 2013. Banded iron formation to iron ore: a record of the evolution of Earth environments? *Geology* 41, 99–102. <https://doi.org/10.1130/G33244.1>.
- Faivre, D., 2016. *Iron Oxides-From Nature to Applications*. Wiley-VCH, Weinheim. <https://doi.org/10.1180/minmag.1992.056.383.20>.
- Fang, J., Ding, B., Gleiter, H., 2011. Mesocrystals: syntheses in metals and applications. *Chem. Soc. Rev.* 40, 5347–5360. <https://doi.org/10.1039/c1cs15043j>.
- Guo, H., Barnard, A.S., 2013. Naturally occurring iron oxide nanoparticles: morphology, surface chemistry and environmental stability. *J. Mater. Chem. A* 1, 27–42. <https://doi.org/10.1039/C2TA00523A>.
- Hagemann, S., Rosière, C., Gutzmer, C., Beukes, N.J., 2008. Banded iron formation-related high-grade iron ore. *Rev. Econ. Geol.*
- Hagemann, S.G., Angerer, T., Duuring, P., Rosière, C.A., Figueiredo e Silva, R.C., Lobato, L., Hensler, A.S., Walde, D.H.G., 2016. BIF-hosted iron mineral system: a review. *Ore Geol. Rev.* 76, 317–359. <https://doi.org/10.1016/j.oregeorev.2015.11.004>.
- Hill, R.J., Howard, C.J., 1987. Quantitative phase analysis from neutron powder diffraction data using the Rietveld method. *J. Appl. Crystallogr.* 20, 467–474. <https://doi.org/10.1107/S0021889887086199>.
- Israelachvili, J.N., 2011. *Intermolecular and Surface Forces*, 3rd ed. Elsevier.
- Kneeshaw, M., Kepert, D.A., 2002. Genesis of high-grade hematite orebodies of the Hamersley province, western australia—a discussion. *Econ. Geol.* 97, 173–176.
- Ko, C.H., Elimelech, M., 2000. The “shadow effect” in colloid transport and deposition dynamics in granular porous media: Measurements and mechanisms. *Environ. Sci. Technol.* 34, 3681–3689. <https://doi.org/10.1021/es0009323>.
- Köhler, P., Kischewitz, J., 2014. Colour chart - Establishing the causes of colouring in iron oxide pigments. *Eur. Coat. J.* 1, 24–28.
- Kuznar, Z.A., Elimelech, M., 2007. Direct microscopic observation of particle deposition in porous media: role of the secondary energy minimum. *Colloids Surf., A* 294, 156–162. <https://doi.org/10.1016/j.colsurfa.2006.08.007>.
- Lascelles, D.F., 2012. Banded iron formation to high-grade iron ore: a critical review of supergene enrichment models. *Aust. J. Earth Sci.* 59, 1105–1125.
- Leite, E.R., Ribeiro, C., 2012. Crystallization and growth of colloidal nanocrystals. Springer. <https://doi.org/10.1007/978-1-4614-1308-0>.
- Liu, J., Miller, J.D., Yin, X., Gupta, V., Wang, X., 2014. Influence of ionic strength on the surface charge and interaction of layered silicate particles. *J. Colloid Interface Sci.* 432, 270–277. <https://doi.org/10.1016/j.jcis.2014.06.028>.
- MacLeod, W.N., 1996. *The geology and iron deposits of the Hamersley Range area, Western Australia*. Geol. Survey West. Austral. Bull.
- Madden, A.S., Hamilton, V.E., Madden, M.E.E., Larson, P.R., Miller, M.A., 2010. Low-temperature mechanism for formation of coarse crystalline hematite through nanoparticle aggregation. *Earth Planet. Sci. Lett.* 298, 377–384. <https://doi.org/10.1016/j.epsl.2010.08.014>.
- McDowell-Boyer, L.M., 1992. Chemical mobilization of micron-sized particles in saturated porous media under steady flow conditions. *Environ. Sci. Technol.* 26, 586–593. <https://doi.org/10.1021/es00027a023>.
- Morris, R.C., 2012. Microplaty hematite – its varied nature and genesis. *Aust. J. Earth Sci.* 59, 411–434. <https://doi.org/10.1080/08120099.2011.626453>.
- Morris, R.C., 2002. Genesis of high-grade hematite orebodies of the Hamersley Province, Western Australia - A discussion. *Econ. Geol.* 97, 177–181.
- Morris, R.C., 2003. Iron ore genesis and post-ore metasomatism at Mount Tom Price. *Appl. Earth Sci.* 112, 56–67. <https://doi.org/10.1179/037174503225011216>.
- Morris, R.C., 1985. Genesis of iron ore in banded iron-formation by supergene and supergene-metamorphic processes – a conceptual model. In: Wolf, K.H. (Ed.), *Handbook of Stratabound and Stratiform Ore Deposits*. Elsevier, Amsterdam. <https://doi.org/10.1016/B978-0-444-42497-6.50006-0>.
- Morris, R.C., 1980. A textural and mineralogical study of the relationship of iron ore to banded iron-formation in the Hamersley iron province of Western Australia. *Econ. Geol.* 75, 184–209. <https://doi.org/10.2113/gsecongeo.75.2.184>.
- Morris, R.C., Fletcher, A.B., 1987. Increased solubility of quartz following ferrous-ferric iron reactions. *Nature* 330, 558–561.
- Morris, R.C., Kneeshaw, M., 2011. Genesis modelling for the Hamersley BIF-hosted iron ores of Western Australia: a critical review. *Aust. J. Earth Sci.* 58, 417–451. <https://doi.org/10.1080/08120099.2011.566937>.
- Niederberger, M., Cölfen, H., 2006. Oriented attachment and mesocrystals: Non-classical crystallization mechanisms based on nanoparticle assembly. *PCCP* 8, 3271–3287. <https://doi.org/10.1039/B604589H>.
- Paris, O., 2008. From diffraction to imaging: New avenues in studying hierarchical biological tissues with x-ray microbeams. *Biointerphases* 3, FB16–26. <https://doi.org/10.1116/1.2955443>.
- Paris, O., Li, C., Siegel, S., Weseloh, G., Emmerling, F., Riesemeier, H., Erko, A., Fratzl, P., 2007. A new experimental station for simultaneous X-ray microbeam scanning for small- and wide-angle scattering and fluorescence at BESSY II. *J. Appl. Crystallogr.* 40, 466–470.
- Patra, A.K., Kundu, S.K., Bhaumik, A., Kim, D., 2016. Morphology evolution of single-crystalline hematite nanocrystals: magnetically recoverable nanocatalysts for enhanced facet-driven photoredox activity. *Nanoscale* 8, 365–377. <https://doi.org/10.1039/C5NR06509G>.
- Patterson, A.L., 1939a. The Scherrer formula for X-ray particle size determination. *Phys. Rev.* 56, 978–982.
- Patterson, A.L., 1939b. The diffraction of X-rays by small crystalline particles. *Phys. Rev.* 56, 972–977.
- Penn, R.L., Banfield, J.F., 1998. Imperfect oriented attachment: dislocation generation in defect-free nanocrystals. *Science* 281, 969–971. <https://doi.org/10.1126/science.281.5379.969>.
- Penn, R.L., Oskam, G., Strathmann, T.J., Searson, P.C., Stone, A.T., Veblen, D.R., 2001. Epitaxial assembly in aged colloids. *J. Phys. Chem. B* 105, 2177–2182. <https://doi.org/10.1021/jp003570u>.
- Pickard, A.L., 2002. SHRIMP U-Pb zircon ages of tuffaceous mudrocks in the Brockman Iron Formation of Hamersley Range, Western Australia. *Aust. J. Earth Sci.* 49, 491–507. <https://doi.org/10.1046/j.1440-0952.2002.00933.x>.
- Powell, C.M., Oliver, N.H.S., Li, Z.X., Martin, D.M., Ronaszeki, J., 1999. Synorogenic hydrothermal origin for giant Hamersley iron oxide ore bodies. *Geology* 27, 175–178. [https://doi.org/10.1130/0091-7613\(1999\)027<0175:SHOFGH>2.3.CO;2](https://doi.org/10.1130/0091-7613(1999)027<0175:SHOFGH>2.3.CO;2).
- Rasmussen, B., Fletcher, I.R., Muhling, J.R., Thorne, W.S., Broadbent, G.C., 2007. Prolonged history of episodic fluid flow in giant hematite ore bodies: Evidence from in situ U-Pb geochronology of hydrothermal xenotime. *Earth Planet. Sci. Lett.* 258, 249–259. <https://doi.org/10.1016/j.epsl.2007.03.033>.
- Rasmussen, B., Krapež, B., Muhling, J.R., Suvorova, A., 2015. Precipitation of iron silicate nanoparticles in early Precambrian oceans marks Earth's first iron age. *Geology* 43, 303–306. <https://doi.org/10.1130/G36309.1>.
- Rasmussen, B., Muhling, J.R., Suvorova, A., Krapež, B., 2016. Dust to dust: evidence for the formation of “primary” hematite dust in banded iron formations via oxidation of iron silicate nanoparticles. *Precamb. Res.* 284, 49–63. <https://doi.org/10.1016/j.precamres.2016.07.003>.
- Rietveld, H.M., 1969. A profile refinement method for nuclear and magnetic structures. *J. Appl. Crystallogr.* 2, 65–71. <https://doi.org/10.1107/S0021889869006558>.
- Rodriguez-Carvajal, J., 2001. Recent developments of the program FULLPROF. *Commission on powder diffraction (IUCr). Newsletter* 26, 12–19.
- Rout, K., Mohapatra, M., Layek, S., Dash, A., Verma, H.C., Anand, S., 2014. The influence of precursors on phase evolution of nano iron oxides/oxyhydroxides: optical and magnetic properties. *New J. Chem.* 38, 3492. <https://doi.org/10.1039/C4NJ00526K>.
- Ryan, J.N., Elimelech, M., 1996. Colloid mobilization and transport in groundwater. *Colloids Surf., A* 107, 1–56.
- Saleh, N., Kim, H.J., Phenrat, T., Matyjaszewski, K., Tilton, R.D., Lowry, G.V., 2008. Ionic strength and composition affect the mobility of surface-modified Fe 0 < nanoparticles in water-saturated sand columns. *Environ. Sci. Technol.* 42, 3349–3355. <https://doi.org/10.1021/es071936b>.
- Smith, R.E., Perdrix, J.L., Parks, T.C., 1982. Burial metamorphism in the Hamersley basin, Western Australia. *J. Petrol.* 23, 75–102. <https://doi.org/10.1093/petrology/23.1.75>.
- Sun, S., Konhauser, K.O., Kappler, A., Li, Y.L., 2015. Primary hematite in Neoproterozoic to Paleoproterozoic oceans. *Bull. Geol. Soc. Am.* 127, 850–861. <https://doi.org/10.1130/B31122.1>.
- Sun, S., Li, Y.L., 2017. Geneses and evolutions of iron-bearing minerals in banded iron formations of > 3760 to ca. 2200 million-year-old: Constraints from electron microscopic, X-ray diffraction and Mössbauer spectroscopic investigations. *Precamb. Res.* 289, 1–17. <https://doi.org/10.1016/j.precamres.2016.11.010>.
- Taylor, D., Dalstra, H.J., Harding, A.E., Bradbent, G.C., Barley, M.E., 2001. Barley Genesis of high grade hematite orebodies of the Hamersley province, Western Australia. *Econ. Geol.* 96–4, 837–873. <https://doi.org/10.2113/gsecongeo.96.4.837>.
- Thorne, W., Hagemann, S., Vennemann, T., Oliver, N., 2009. Oxygen isotope compositions of iron oxides from high-grade BIF-hosted iron ore deposits of the central Hamersley Province, Western Australia: constraints on the evolution of hydrothermal fluids. *Econ. Geol.* 104, 1019–1035.
- Thorne, W.S., Hagemann, S.G., Barley, M., 2004. Petrographic and geochemical evidence for hydrothermal evolution of the North Deposit, Mt Tom Price, Western Australia. *Miner. Deposita* 39, 766–783. <https://doi.org/10.1007/s00126-004-0444-x>.
- Thorne, W.S., Hagemann, S.G., Barley, M.E., 2006. Hydrothermal alteration zonation and fluid chemistry of the Southern Ridge and North deposits at Mt Tom Price. *Appl. Earth Sci.* 115, 152–160. <https://doi.org/10.1179/174327506X139011>.
- Thorne, W.S., Hagemann, S.G., Sepe, D., Dalstra, H.J., Banks, D.A., 2014. Structural control, hydrothermal alteration zonation, and fluid chemistry of the concealed, high-grade 4EE iron orebody at the paraburdoo 4E deposit, Hamersley Province, Western Australia. *Econ. Geol.* 109, 1529–1562. <https://doi.org/10.2113/econgeo.109.6.1529>.
- Thorne, W.S., Hagemann, S.G., Webb, A., Clout, J., 2008. Banded iron formation-related iron ore deposits of the Hamersley Province, Western Australia. *Rev. Econ. Geol.* 15, 197–221.
- Tong, M., Johnson, W.P., 2006. Excess colloid retention in porous media as a function of colloid size, fluid velocity, and grain angularity. *Environ. Sci. Technol.* 40, 7725–7731. <https://doi.org/10.1021/es061201r>.
- Tosco, T., Bosch, J., Meckenstock, R.U., Sethi, R., 2012. Transport of ferrihydrite nanoparticles in saturated porous media: Role of ionic strength and flow rate. *Environ. Sci. Technol.* 46, 4008–4015. <https://doi.org/10.1021/es202643c>.
- Tosco, T., Tiraferri, A., Sethi, R., 2009. Ionic strength dependent transport of micro-particles in saturated porous media: Modeling mobilization and immobilization phenomena under transient chemical conditions. *Environ. Sci. Technol.* 43,

- 4425–4431.
- Trendall, A.F., Blockley, J.G., 1970. The iron formations of the Precambrian Hamersley Group Western Australia. *Geol. Surv. Western Australia Bull.* 119.
- Trendall, A.F., Compston, W., Nelson, D.R., De Laeter, J.R., Bennett, V.C., 2004. SHRIMP zircon ages constraining the depositional chronology of the Hamersley Group, Western Australia. *Aust. J. Earth Sci.* 51, 621–644. <https://doi.org/10.1111/j.1400-0952.2004.01082.x>.
- Webb, A.D., Dickens, G.R., Oliver, N.H.S., 2004. Carbonate alteration of the Upper Mount McRae Shale beneath the martite-microplaty hematite ore deposit at Mount Whaleback, Western Australia. *Miner. Deposita* 39, 632–645. <https://doi.org/10.1007/s00126-004-0434-z>.
- Zhang, J., Huang, F., Lin, Z., 2010. Progress of nanocrystalline growth kinetics based on oriented attachment. *Nanoscale* 2, 18–34. <https://doi.org/10.1039/B9NR00047J>.